Ultrasonics Sonochemistry 83 (2022) 105950

Contents lists available at ScienceDirect

Ultrasonics Sonochemistry

journal homepage: www.elsevier.com/locate/ultson

Hydrodynamic cavitation for micropollutant degradation in water – Correlation of bisphenol A degradation with fluid mechanical properties

Manuel Deggelmann [a,b], Julius-Alexander Nöpel [c], Frank Rüdiger [c], Dirk Paustian [a,b], Patrick Braeutigam [a,b,d,*]

[a] Institute of Technical and Environmental Chemistry, Friedrich Schiller University Jena, Philosophenweg 7a, 07743 Jena, Germany
[b] Center for Energy and Environmental Chemistry (CEEC Jena), Friedrich Schiller University Jena, Philosophenweg 7a, 07743 Jena, Germany
[c] Institute of Fluid Mechanics, Faculty of Mechanical Science and Engineering, Technische Universität Dresden, George-Baehr-Str. 3c, 01069 Dresden, Germany
[d] Fraunhofer IKTS, Fraunhofer Institute for Ceramic Technologies and Systems, Michael-Faraday-Straße 1, 07629 Hermsdorf, Germany

ARTICLE INFO

Keywords:
Hydrodynamic cavitation
Bisphenol A
Micropollutants
Fluid mechanical properties
Optical measurements
Chemiluminescence

ABSTRACT

The present work addresses the correlation of bisphenol A (BPA) degradation by hydrodynamic cavitation with the fluid mechanical properties of the cavitating jet in the reactor. The effects of inlet pressure and two orifices were investigated. The fluid mechanics conditions during the reaction were evaluated by optical measurements to determine the jet length, bubble volume, number of bubbles, and bubble size distribution. In addition, chemiluminescence of luminol is used to localize chemically active bubbles due to the generation of hydroxyl radicals in the reactor chamber. The correlation between the rate constants of BPA degradation and the mechanical properties of the liquid is discussed. Here, linear dependencies between the degradation of BPA and the volume expansion of the bubble volume and chemiluminescence are found, allowing prediction of the rate constants and the hydroxyl radicals generated. BPA degradation of 50% was achieved in 30 min with the 1.7 mm nozzle at 25 bar. However, the 1 mm nozzle has been demonstrated to be more energetically efficient, achieving 10% degradation with 30% less power per 100 passes. There is a tendency for the number of small bubbles in the reactor to increase with smaller nozzle and increasing pressure difference.

1. Introduction

The effect of hydrodynamic cavitation (HC) is well known in the field of fluid mechanics. Cavitation is responsible for the erosion of ship propellers, pumps and water turbines, for instance [1–3]. The phenomenon occurs due to an increase in flow velocity leading to a decrease in local pressure. The decrease in local pressure down to vapour pressure results in the formation of vapour and gas filled bubbles. When the pressure increases, bubbles implode [4,5].

The collapse of the bubbles causes locally extreme temperatures, pressures, and heat transfer with high physical stress to materials in the fluid and near to surfaces (so-called microjet) [2,6]. The collapse of cavitating bubbles creates hot spots [7], which cause cleavage of water molecules, thus forming hydroxyl radicals Eq. (1). The radicals possess a high oxidation potential [8], which enables the radicals to attack organic pollutants in water and degrade them over multiple oxidation steps [9] to form lower molecular weight compounds [10,11].

$$H2O \xrightarrow{)))} \cdot OH + \cdot H \quad (1)$$

Besides the formation of radicals, the implosion of collapsing bubbles generates strong pressure waves, which in turn are used for physical and chemical processes such as emulsification [12,13], biodiesel synthesis [14], biomass pre-treatment [15], disinfection [16,17] and treatment of waste water and real industrial effluent [18,19].

Hydrodynamic cavitation used for the treatment of contaminated water has attracted much attention in recent years. In water treatment technology, other processes such as ozone [20,21], Fenton [22,23], photocatalytic oxidation [24,25] and ultrasound are widely used [26–28]. All of these processes, including hydrodynamic cavitation, are classified as advanced oxidation processes (AOP).

Reasons for the lack of attention to cavitation are the relatively low degradation performance [29] and the very complex fluid mechanical properties of the bubbles [30], which are not yet understood in detail. However, it is known that thermodynamic state variables such as pressure and temperature have a large influence on the bubble dynamics, but

* Corresponding author at: Institute of Technical and Environmental Chemistry, Friedrich Schiller University Jena, Philosophenweg 7a, 07743 Jena, Germany.
E-mail address: patrick.braeutigam@uni-jena.de (P. Braeutigam).

https://doi.org/10.1016/j.ultsonch.2022.105950
Received 31 July 2021; Received in revised form 29 January 2022; Accepted 5 February 2022
Available online 9 February 2022

also the type of cavitation generator, e.g. venturi or orifice plate, and the reactor geometry, the gas fraction and the materials to be degraded. The influence of these parameters is complex and interdependent [31]. Nevertheless, processes using hydrodynamic cavitation have some advantages, such as low production cost of cavitation equipment [32], easy scale-up, no addition of other chemicals, and the possibility of combination with other processes [33,34].

The research groups of Pandit and Gogate published numerous studies on the use of HC in water treatment with various pollutants and equipment. In an early work, they optimized the parameters of pressure and geometry of an orifice [35]. In addition, research was conducted in [36,37] for optimized cavitation degradation for many pollutants, studies to increase the efficiency and conversion in the HC process, and HC in combination with other AOPs [38–41]. In most cases, venturi nozzles or orifice plates have been used as cavitation generators.

During the investigations, optimum values for geometric variables and process conditions could be specified for the related configurations. Pandit et al. found an optimum inlet pressure at $p_1 = 4$ bar to $p_1 = 6$ bar with an outlet pressure of nearly ambient pressure. Dular et al. uses different systems to generate HC (Venturi, shear induced HC reactor) [19]. The experiments were carried out with a 'shear-induced' cavitation reactor and a venturi set-up with restrictions from $d = 15$ mm to $d = 1$ mm. It was observed that HC is suitable for removal of pharmaceuticals and cyanobacteria with pressure levels below $\Delta p = 10$ bar. Angaji et al. used for water decontamination of dimethylhyrazine a multi hole orifice system [42]. At inlet pressure of $p_1 = 6.5$ bar and a downstream pressure of $p_2 = 3$ bar optimal degradation of the pollutant takes place. After 120 min treatment time 98.6% of dimethylhydrazine was degraded. In summary, it can be noted that the publications of all groups dealing with water treatment by HC use inlet pressures below $p_1 = 10$ bar.

In the present paper, a higher pressure range from $\Delta p = 10$ to $\Delta p = 30$ bar is investigated. In addition to analysing the pressure dependence, the effects of different sized orifice diameters are also explored. In addition, as a novelty, a relationship between the mechanical properties of the cavitating flow, in particular the extent of jet cavitation and the bubble characteristics in the reactor, and the degradation differences are investigated.

Optimal operating points of strongest cavitation with glass venturi tube were determined by Soyama and Hoshino using optical images of bubble fields and measurement of acoustic power and luminescence [43]. For this purpose, a range of $p_1 = 4$ to $p_1 = 6$ bar was employed for the inlet pressure and a range of $p_2 = 1.2$ bar to $p_2 = 3$ bar for the outlet pressure. It was found that maximum cavitation intensity occurs when a suitable ratio of inlet and outlet pressure is set. The optimum downstream pressure increases with increasing inlet pressure. For $p_1 = 6.0$ bar, an optimum downstream pressure of $p_2 = 2.3$ bar was determined. The luminescence results showed a maximum at the same operating point.

Schlender et al. also applied optical methods for the acquisition of chemiluminescence. Using this method, the flow reactivity or the intensity of hydrodynamic cavitation at different pressures upstream and downstream of the nozzle can be analysed [44]. They used a two-stage nozzle system for homogenization processes of oil droplets in water. Bubble collapse intensity measured by chemiluminescence was correlated with emulsification results. The method of chemiluminescence, as used by Schlender et al. is a well-known application that visualizes ultrasonic fields [45]. In this method, the luminol molecule is excited to emit light by reacting with hydroxyl radicals, thus visualizing reactive regions in the flow.

In comparison with the above studies in aqueous systems, the effects of cavitation in valves and chokes of hydraulic systems were investigated by optical methods [46,47]. Here, for different pressure levels, the numerous gas bubbles generated by HC could be measured by their size and distribution. Effects due to outgassing have an influence on the degradation of substances [30,48].

In this study, BPA is used as a model substance for organic pollutants at low concentration (0.25 μmol/l). BPA is produced in large quantities for industrial use in plastics and epoxy resins [49]. Due to its wide range of applications, BPA is ubiquitous in water bodies. BPA exhibits relatively high stability to microorganisms and is poorly degraded in wastewater treatment plants [50]. BPA is hazardous to aquatic animals and to humans because it is known to be an endocrine disruptor [51,52]. The development of efficient elimination processes is therefore an important necessity.

In the literature, there are studies with different methods for the degradation of BPA. The AOP related treatments for BPA are performed with single methods and combinations of techniques by photodecomposition – effective in TOC reduction and BPA degradation of 95% over hours [53], ozone – BPA degradation as a function of ozone doses, possibility of fully reduction [21], electrochemical oxidation combined with acoustic cavitation – reduction of 90% in 30 min [54] or with chlorination [55], Fenton process with and without additional sonochemical treatment [23], a combination of HC and persulfate oxidation – optimal pressure of 5 bar over 2 h with 89,7% degradation [32]. Others conducted studies using only acoustic cavitation – with high COD and TOC reduction rates over 50% and 80% by 1,7 MHz [56] and treatments of 1 h by 300 kHz resulting of fully degradation in 1 h using 150 ml [57]. In [58] only HC with optimal pressure of 3 bar is used. After treatment of 3 h using a multi hole plate with $d = 1$ mm (orifice) 27,6% BPA reduction was achieved. For continuous treatment of water contaminated with BPA, HC with a relatively high flow rate is the most practical.

The novelty of this work presented here is the connection of the fluid mechanical properties of hydrodynamic cavitation in a higher pressure range compared to the literature. For this purpose, the properties of the cavitating jet, bubble characteristics and chemiluminescence are correlated with the degradation rates of BPA in water. Most studies use the methods presented above and optimize the process in terms of degradation performance. However, the degradation rate directly depends on the spatial distribution and the size of the bubbles, which are generated in-situ in the respective reactor.

In this study, the cavitation jet, generated by the single orifice plate, and the bubbles in the reactor chamber are analysed using optical measurement techniques. For this purpose, optical images are acquired in the reactor using laser light sheet and high-speed camera. For the chemiluminescence of luminol long-term exposure images are recorded. The spatial bubble distribution shows the cavitation region, while the chemiluminescence reveals location of flow reactivity. In addition, the results of the degradation of bisphenol A (BPA) with HC are presented. At the end, the connection of BPA degradation and fluid mechanical properties of the jet is discussed. The aim of this study is showing correlations between the behaviour of the bubble field and the pollutant degradation by HC, which will lead to a better understanding of the fluid mechanical influence parameters in hydrodynamic cavitation for water treatment.

2. Material and methods

2.1. Chemicals

All chemicals were used as received without any further purification. Bisphenol A (4-[2-(4-Hydroxyphenyl)propane-2-yl]phenol, 97% purity), was purchased from Alfa Aesar and luminol (5-Amino-2,3-dihydro-1,4-phthalazinedione) (>95% purity) from AppliChem. Sodium carbonate (>99% purity) were purchased from Merck and methanol (HPLC-grade) was supplied by VWR. Deionized water (3 μS cm^{-1}) was used for the preparation of BPA-solutions and ultrapure water (Λ = 0,062 μS cm^{-1}) for HPLC measurement.

2.2. Experimental setup

Experiments were performed in a circular flow system (Fig. 1). The

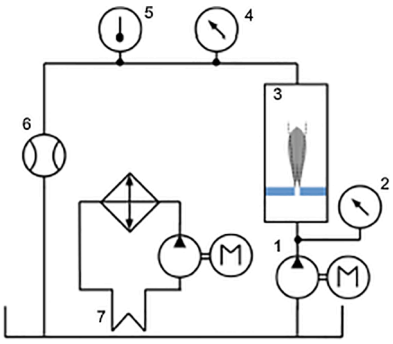

Fig. 1. Experimental setup for investigations on hydrodynamic cavitation. The setup consists of a pump with frequency controller (1), inlet pressure gauge p_1 (2), glassy cavitation chamber with orifice (3), pressure gauge p_2 at reactor chamber outlet (4), temperature probe (5), volumetric flow meter (6) and an open tank with a cooling system (7).

setup comprises a high-pressure pump (HydraCell G03K, *Verder*, Germany), two pressure gauges (inlet pressure p_1 before the orifice and pressure p_2 at the outlet of the reactor), a flow meter, the cavitation reactor and an open tank with a cooling coil inside. The pressure difference Δp is calculated by $\Delta p = p_1 - p_2$. The temperature is set on a constant value of $T = 20 \pm 2$ °C by a refrigerated circulator (FP 50, *Julabo*, Germany).

The cavitation reactor consists of a cylindrical coaxial orifice with a reaction chamber out of a glass cylinder. A sketch of the reactor is shown in Fig. 2. In the present investigation, two orifices with different diameter d (1.0 mm and 1.7 mm) were used. The pipe in front of the orifice has a diameter of 10 mm. The diameter of the reactor chamber is $D = 15$ mm. Downstream the reactor, the pipe is of the same size as the supply pipe. The dimensions of the reactor are summarized in the table of Fig. 2.

The investigations were performed in pressure differences from $\Delta p = 10$ bar to a maximum of $\Delta p = 30$ bar. The Reynolds number Re and the cavitation number Ka are used to characterize the flow Eq. (2):

$$Re = w_0\, d/\nu \; Ka = (p_\infty - p_v)/\Delta p \tag{2}$$

In the calculation of dimensionless numbers, w_0 stands for velocity at orifice exit, ν for the viscosity, p_v for vapour pressure of water and p_∞ for ambient pressure.

For BPA degradation experiments a volume of $V = 500$ ml of BPA solution ($c_0 = 0.25$ µmol/l) was filled in the system circuit. Because of mixing and filling all pipes, the pump was run for $t = 30$ s at low power with no cavitation occurring. After this, the first sample was taken for determination of the initial concentration. A sample has been taken out of the tank at $t = \{0; 5; 10; 15; 30\}$ minutes. It amounted to approx. $V_n = 1$ ml for one test sample. The sample was analysed by HPLC without any further treatment. In addition, experiments without orifice for 1.5 h at operating flow conditions showed no degradation or adsorption effects of BPA.

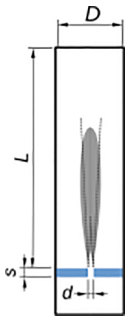

Fig. 2. Sketch of the cylindrical cavitation reactor with length L and diameter D including the size of the stainless steel orifice integrated in the supply pipe with diameter d and thickness s. Dimensions are given in the table on the right.

2.3. Bisphenol A analysis

HPLC measurements for determination the BPA concentration were carried out on a HPLC System (HPLC 2000, *Jasco*, Japan), equipped with a fluorescence detector (FP 2020, *Jasco*, Japan). For the separation, a Kromasil C18 (250 mm × 4.6 mm × 5 µm) column was used and for fluorescence detection an excitation wavelength of $\lambda = 275$ nm and emission wavelength of $\lambda = 305$ nm was chosen. The eluent consisted of two components: A (ultrapure water) and B (methanol) with ratio of A:B 37.5:62.5 (v/v). The analysis was performed at a flow rate of $\dot{V} = 1.5$ ml min^{-1}, a column oven temperature of $T = 40$ °C and $V = 50$ µl of sample was injected into the column. The retention time of BPA was $t = 6$ min. The limit of detection (LOD) was calculated to be 0.47 nmol/l and the limit of quantification (LOQ) to be 1.41 nmol/l.

2.4. Visualization of oxidative species by chemiluminescence

For the visualisation of the oxidative species, $V = 500$ ml of an alkaline luminol solution ($c = 2.0$ g l^{-1} of luminol, $c = 5.0$ g l^{-1} of Na_2CO_3, pH = 10, $V = 1$ ml of hydrogen peroxide solution (30%)) was filled in the system circuit. The chemiluminescence was recorded in darkness with an SLR camera (Canon EOS 1100D, EF-S 18–55 mm IS II lens) at an exposure time of $t_b = 10$ min (ISO 800, 35 mm, F/5.6. The distance between the reactor and the camera sensor was $l_c = 358$ mm. All images were processed equally as it was done in [31]. The images are transformed to binary images evaluating the extent, area and volume of chemiluminescence. For this purpose, a threshold value was defined in such a way that occurring image noise was minimized and the intensity of the emitted light was increased. Specifically, a template was created for an image with high noise and low emitted light and applied to all other images. This ensures comparability. The white pixels, generated by the binary image, represent the region where light was emitted. This corresponds to the area of chemiluminescence. The conversion to binary images leads to the loss of the information about the intensity distribution of the area. With the assumption of a symmetrical formation of the cavitating jet, a volume of chemiluminescence can be determined from the area.

2.5. Measurements of fluid mechanical properties by optical methods

The experimental setup, primarily consisting of the orifice and the reactor chamber, are identical for both, the degradation experiments, and optical measurements. However, for making high-resolution images of the gas bubbles in the reactor some adaptations had to be made. To minimize refraction due to the curvature of the cylinder wall, a quadratic chamber was mounted around the reactor and it was filled with glycerine (85%). For the imaging, a camera was mounted on an optical bench in front of the reactor. Due to the short exposure times required, a Nd:YAG laser was used as the illumination source, which brought a light sheet perpendicular to the image-capturing plane into the reactor. At the bubble-liquid-interfaces, light is reflected. Therefore, the brightness of the images increases with the bubble density. Because of this fact, the lighting by diffuse reflection varies for different flow conditions. For the evaluation of the jet length and the determination of the bubble size 800 images with an acquisition time of $t_b = 25$ µs were taken for each measurement. For image, processing the software *ImageJ* was used.

To identify the jet length, an averaging of the 800 grey scale images was carried out and adjusted by means of a threshold value. The threshold has been defined to minimize image noise and to reveal a bubble field on each image. The unprocessed captured B/W image has low brightness, so the maximum grayscale value is at most half the highest brightness value.

The determination of the bubble size and number was conducted in an area next to the jet, which was located in the recirculation area [48]. In this area, the velocity is smaller by a factor of 10 and the bubble density is low enough to obtain sharp images for every investigated pressure level. The bubbles are identified with *ImageJ,* counted and classified by diameter. The evaluation presented in Section 3.2 shows the average number of bubbles with a certain diameter range per image.

3. Results and discussion

3.1. Cavitating jet

The method of laser light sheet imaging reveals the structure and size of the cavitating jet sharply by short exposure times. To characterize the flow in the reactor at different operating points with the respective pressure differences, the dimensionless numbers *Re* and *Ka* calculated by Eq. (2) are listed in Table 1.

Accordingly, the flow is to be considered highly turbulent and therefore underlies strong temporal and spatial fluctuations. Fig. 3a and b show images of the cavitating jet with orifice $d = 1$ mm and $d = 1.7$ mm at $\Delta p = 30$ bar with an exposure time of $t_b = 25$ µs. For a better assessment of the jet properties, the images were increased in brightness and contrast. Those images are used for further evaluation regarding the length of the jet, bubble amount and size.

Regions with a high bubble density are brighter compared to regions with low density or without bubbles. This is a result of light scattering at the gas-liquid interphase of the bubbles. Fig. 3a and b moreover illustrate that the bubbles collapse after a certain length x from the orifice exit. The length and volume of the bubble field strongly depend on the pressure and the diameter of the orifice. For this purpose, instantaneous images for different boundary conditions, varying pressure and orifices, were recorded. The images illustrate typical jet features, such as the formation of a shear layer, as well as small scale and large-scale vortex structures.

Fig. 4 shows processed images by thresholding which have been averaged from 800 instantaneous frames from the configuration with d = 1 mm varying pressure difference Δp. The captured black area represents the area of the cavitating jet, which are presented for different pressure levels.

From these images, which have been all processed in the same way, volume (V) and depth of penetration (l) of the cavitation cloud is determined.

It becomes apparent that with rising pressure p_1, the ratio of l / d (length of jet normalized with the corresponding orifice diameter) increases, representing the bubble cloud. Looking at the length ratio, a roughly linear increase of the length of the cavitation area occurs up to a pressure of $\Delta p = 25$ bar. After that pressure level, the length ratio barely increases. The limited chamber volume of the cavitation reactor significantly dampens the expansion of the jet at high-pressure levels. The limitation of the expansion of the bubble area by the wall boundary becomes dominant with increasing inlet pressure and with increasing orifice diameter.

In order to generalise the results, the effect of changes in operating conditions are measured by quantities of momentum, hydraulic power and energy of the jet. The momentum flow $\dot{I}$, the power P and the energy E of the jet with $\Delta p = 0.5\ \rho\ w_0^2$ depend again on measured physical quantities such as volume flow $\dot{V}$, pressure difference Δp between p_1 and p_2 and treatment time t_t:

$$\dot{I} = \dot{m} w_0\ \dot{V}\sqrt{\Delta p}\ \dot{V}^2 \tag{3}$$

$$P = \frac{\dot{m}}{2} w_0^2 = \dot{V}\Delta p\ \dot{V}^3 \tag{4}$$

$$E = \frac{\dot{m}}{2} w_0^2 t_t = \dot{V}\Delta p t_t\ t_t \dot{V}^3 \tag{5}$$

with $\dot{m}$ for the mass flow and w_0 as exit velocity of the orifice. The momentum, power and energy are largely independent of the reactor geometry and this provide an opportunity to compare different configurations in this study and investigations of other groups. These quantities are important for the assessment of applied resources to achieve chemical conversion. In addition, the simplifications in Eqs. (3)–(5) illustrate how these basic quantities are dependent on the volume flow.

For comparing the penetration depth of the cavitation field for $d = 1$ mm and $d = 1.7$ mm, Fig. 5a displays the normalized depth of penetration l / d plotted against the normalized velocity w/w_n. The bulk velocity at the orifice exit is normalized with the minimum velocity w_n, which represents the state at lowest possible pressure Δp in the reactor chamber, where cavitation begins to occur. The beginning of the cavitation was evaluated visual and acoustical and the volume flow was recorded at this minimum pressure p_m in order to determine the minimum velocity for normalization. The minimum pressure corresponds to $p_m = 2$ bar for both orifice configurations.

For the comparison with a non-cavitating water jet from literature, the calculation of the single-phase flow with the orifice exit velocity w_d, the low pressure difference of $\Delta p = 10$ bar for $d = 1.7$ mm with a relatively low bubble density was used as a reference in order to determine the velocity at the end of the cavitation field w_l from the length of the cavitation field l with the formula

$$\frac{w_l}{w_d} = \frac{6.2}{l} d \tag{6}$$

for a single-phase, free jet according to [59]. It was then used as a reference velocity where the cavitating bubbles dissolve. From this, the length of a single-phase turbulent free jet was calculated.

The jet penetration depth l normalized with the diameter d of the orifice is greater for $d = 1$ mm compared to the larger orifice $d = 1.7$ mm. Moreover, the slope of the curves shown in Fig. 5a is steeper for the smaller orifice. This is also shown by the difference between the growth of the normalized jet lengths between $\Delta p = 10$ bar and $\Delta p = 25$ bar. While in this range at $d = 1$ mm the ratio l / d increases by a factor of 3, at $d = 1.7$ mm the ratio only increases by a factor of 2.

Comparing the results of both orifice configurations one has to take in mind the fact that the penetration length of the jet depends on the relation between inertia and friction, representation by the surface area and cross-sectional area of the jet. In the occurrence of cavitation, only the friction changes, because the bubble formation in the orifice appears at the wall and in the shear layer of the jet. This leads to the hypothesis that the relation between the penetration lengths is inverse proportional to the diameter of the orifice, $(l_1/d_1)/(l_2/d_2) \sim d_2/d_1$.

Without the normalisation of the length of visible cavitation by d, at same pressure levels the field with $d = 1.7$ mm would in principle be longer compared to $d = 1$ mm orifice. Because of the limited volume of the reactor, the difference of the jet length distance between the two orifices Δl decreases with rising pressure. This becomes apparent by looking at the length l of each configuration only. From this perspective it becomes clear that at $\Delta p = 10$ bar the difference between $d = 1$ mm und $d = 1.7$ mm is larger than at $\Delta p = 25$ bar.

Table 1
The dimensionless numbers associated with the operating points of the d = 1.0 mm and d = 1.7 mm orifices: Reynolds number Re and Cavitation number Ka.

Pressure difference Δp in bar	Reynolds number *Re* for $d = 1$ mm	Reynolds number *Re* for $d = 1.7$ mm	Cavitation number *Ka*
5	24,620	35,740	0.2
10	31,410	49,420	0.1
15	37,290	61,000	0.06
20	43,170	71,400	0.05
25	49,050	77,010	0.04
30	52,650	87,460	0.03

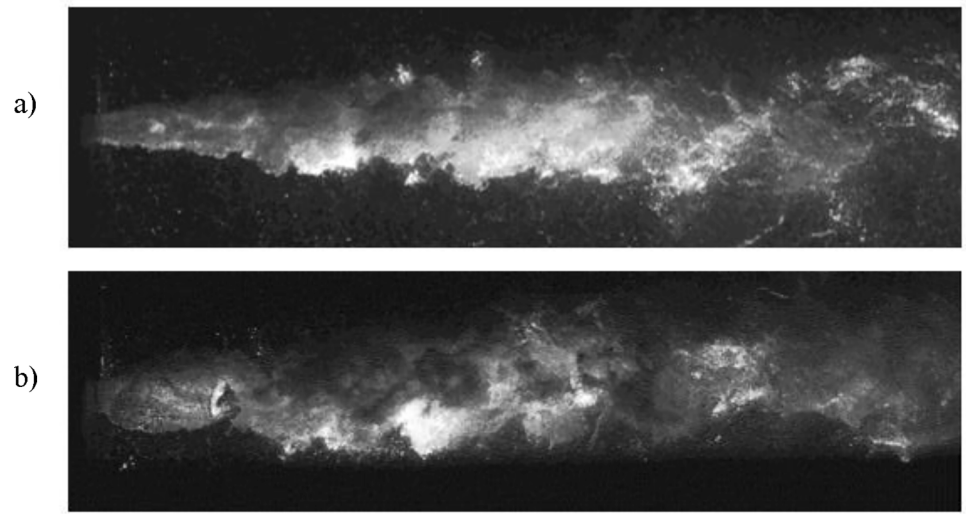

Fig. 3. Instantaneous images of a section of the reactor with the entering cavitating jet at Δp = 30 bar gained by laser light sheet method with an exposure time of t_b = 25 µs. a) d = 1 mm (Re = 52,647; Ka = 0.03), b) d = 1.7 mm (Re = 87,463; Ka = 0.03). Images are brightened and contrasted.

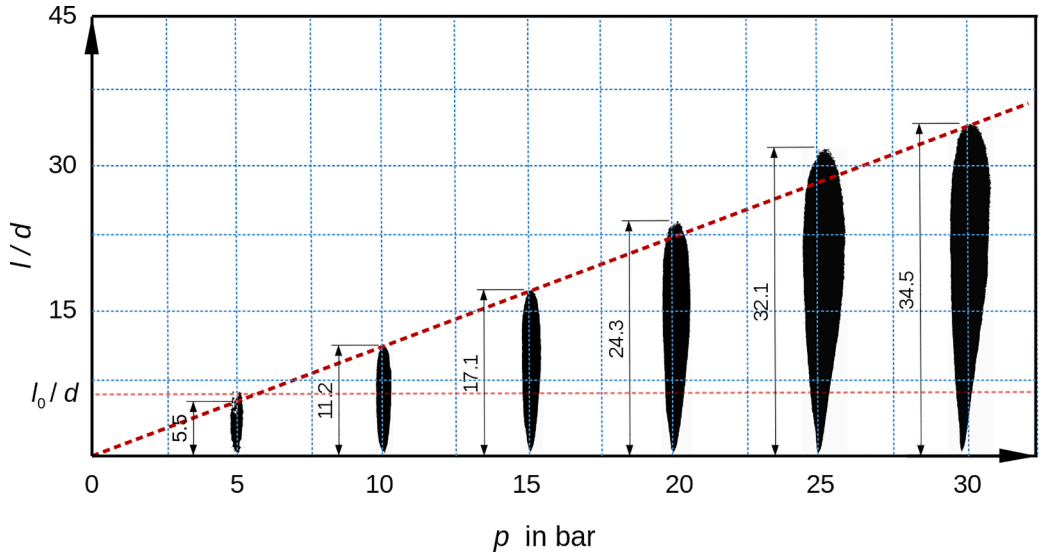

Fig. 4. Comparison of the length ration l/d of the averaged shapes of the cavitation field at different pressure Δp for d = 1 mm acquired by using a laser light sheet method (averaged shape obtained from 800 instantaneous frames per pressure level).

When comparing the $d = 1$ mm configuration with cavitation to the calculated values of a single-phase turbulent free jet, significant differences result. Especially the difference with the $d = 1$ mm orifice is significant. It can be explained due to the different densities of the single-phase and the cavitating multi-phase fluid jet. A single-phase turbulent water jet has a higher density than a cavitating jet, due to the high amount of bubbles. Because of the reduced mass resulting from the lower density of the cavitating bubble jet, the volume accelerates more strongly because the inertia of the cavitating bubble volume is lower. As a result, the jet penetrates deeper into the reactor. If the inlet pressure p_1 rises, the amount of gas bubbles rises, thus, the length of the cavitation field increases. Therefore, it can be assumed that with rising inlet pressures the decay rates of the velocity of the jet decreases as the amount of bubbles increases. In addition, the length difference between the single-phase and the cavitating multi-phase flow with $d = 1.7$ mm is clearly smaller. The reason for this is, on the one hand, the limitation of the reactor volume, which prevents an expansion of the cavitation jet. This is particularly evident at pressure levels above $\Delta p = 15$ bar for $d = 1.7$ mm and at $\Delta p = 30$ bar for $d = 1$ mm and strongly depends on reactor geometry. Another reason should be that for the smaller orifice the bubble amount and thus the gas fraction with respect to the volume flowing through the orifice is higher than for the larger orifice. The bubble amount and sizes are discussed in more detail in Section 3.2 below. When comparing the cavitating jets with nozzle diameters of $d = 1.7$ mm at 10 bar and 20 bar pressure difference with jet length measurements by Soyama [60], it can be stated that they are almost identical at the same cavitation numbers.

In order to establish a relation between bubble field and degradation, it is important to examine the bubbly volume V generated by an applied hydraulic power P. Fig. 5b displays the proportion of the volume to the reactor volume, V/V_R, against the hydraulic power P. At first it is clearly visible that with $d = 1$ mm larger volume fraction of bubbles are produced at lower power levels. The rise between pressure $\Delta p = 5$ bar (point of lowest power P) and $\Delta p = 25$ bar (second highest power) is very strong, whereas with $d = 1.7$ mm the curve has an exponentially decaying shape. This is due to the limitation of the volume of the cavitation reactor chamber, which becomes also clear with $d = 1$ mm when the pressure exceeds $\Delta p = 25$ bar. For $d = 1.7$ mm it is already noticeable

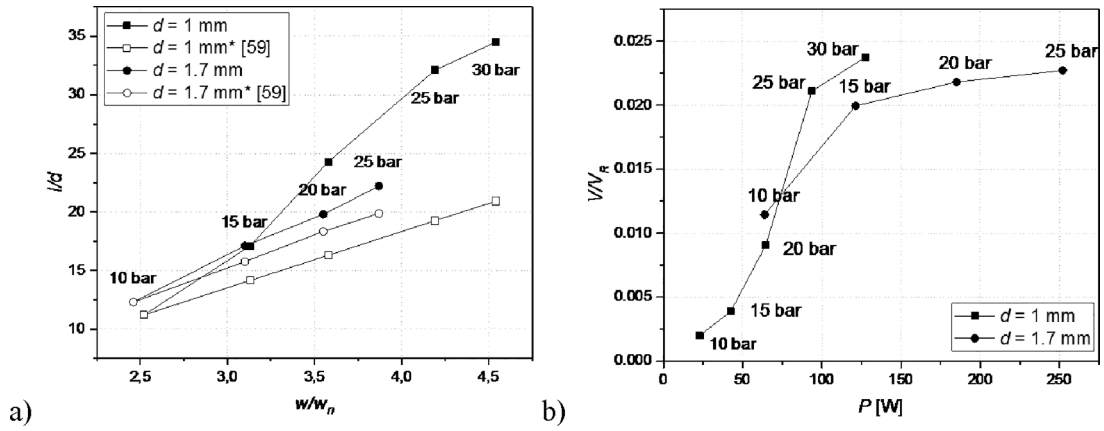

Fig. 5. Expansion of the cavitation field illustrated by penetration length and the bubble volume. a) Normalized depths of jet penetration l / d for the configuration with d = 1 mm and d = 1.7 mm plotted over the normalized velocity w/w_n. The curve of 1 mm* and 1.7 mm* shows the calculated length of a single-phase water jet [59]. b) Cavitation cloud volume of the cavitating jet V assuming rotational symmetry, normalized with the reactor volume V_R, over the hydraulic power P for both orifice configurations. Data from processed images gained by laser light sheet method (averaged images from 800 instantaneous frames). Points connected by linear trend lines.

when the pressure rises above $\Delta p = 15$ bar. By the limitation, the jet is strongly narrowed with the larger orifice, which resembles with a resistance. This leads to stronger circulation, the pressure gradient in the direction of the jet is steeper and the shear must be higher. This should lead to higher degradation.

It has to be mentioned that the averaged shadow images with a fixed threshold value are narrower in the area after the orifice for pressures above $\Delta p = 20$ bar in the configuration with $d = 1.7$ mm and therefore the area is smaller, which is directly reflected in the volume of the cavitating jet. Therefore, these values should be treated with caution. The data provide information on trends and global effects. Exact statements about the quantity are inappropriate with this method.

3.2. Amount of bubbles and distribution of bubble size

To determine the local conditions of the cavitating jet, the amount and size of bubbles are of great interest. The difficulty of determining these values lies in the physics of the jet, because the jet consists of very small and fast moving bubbles. This results in a strongly overlap of bubbles in the images. The difficulty of directly determining these values in the jet is discussed in [48]. For the estimation of the dependence of the bubble size and amount on the inlet pressure it is, however, possible to observe them in the recirculation area next to the jet. Reference is made to the results in [48].

It was found that for both orifice configurations, with increasing inlet pressure the total number of bubbles increases, shown in Fig. 6. In the tabular listing below the bar graph, the number of bubbles for three different classes of bubble diameters are displayed. It can be seen, that the amount of bubbles is much higher for the $d = 1$ mm compared to $d = 1.7$ mm. The main contribution comes from the change of bubbles in the class smaller than $d_b = 50$ µm. It increases for the smaller orifice by rising pressure significantly but not so strong for $d = 1.7$ mm. This has a great impact on the amount at all. In Fig. 6 the listing shows, that almost no bubbles with diameters $d_b > 0.175$ mm occur for $d = 1$ mm and pressures levels above $\Delta p = 20$ bar, but for $d = 1.7$ mm bigger bubbles are formed. The coalescence rate is higher for the larger orifice due to the stronger shear since the volume of the reactor limits the expansion of the jet.

The following hypotheses can be derived from the expectations of the flow:

I) The degradation should rise by increasing inlet pressure, since volume flow increases and thereby the minimum pressure in the orifice decreases, resulting in more and smaller bubbles and thus

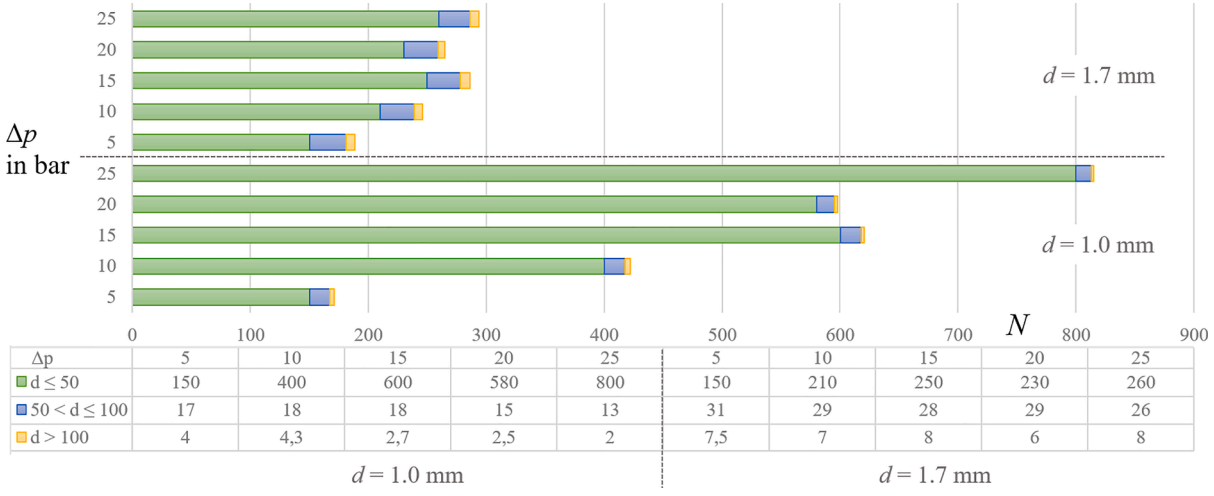

Δp	5	10	15	20	25	5	10	15	20	25
d ≤ 50	150	400	600	580	800	150	210	250	230	260
50 < d ≤ 100	17	18	18	15	13	31	29	28	29	26
d > 100	4	4,3	2,7	2,5	2	7,5	7	8	6	8
	d = 1.0 mm					d = 1.7 mm				

Fig. 6. Display of amount and size of bubbles according to three different categories of diameter for the configurations studied. The number N represents the number of bubbles per image averaged from 800 single frames.

leading to a stronger bubble collapse with locally higher pressure and temperature. In addition, more fluid is treated in time.

II) The limitation of the expansion of the jet at $d = 1.7$ mm leads to a stronger pressure increase in the direction of the main flow, which in turn influences the bubble implosions. Due to this volume limitation, the flow mixes more strongly, especially at high inlet pressures for the bigger orifice. Higher shear and degradation rates should be expected. On the other hand, the limitation results in an increase of the intensity of recirculation and thus coalescence of the bubbles, which can lead to larger bubbles reducing degradation. There is an operating point where degradation occurs efficiently.

III) A larger orifice diameter provides a higher volume flow. More volume per time can be treated by cavitation. This leads to a higher conversion in a certain time but requires more power.

3.3. Chemiluminescence of luminol

Cavitation bubble collapse in water lead to formation of radicals such as ·OH [7]. A spatial distribution of hydroxyl radicals is required for a more precise analysis of the conversion areas in hydrodynamic cavitation. For this purpose, the light emission of luminol reacting with hydroxyl radicals is used. The blue light emission during this reaction is called chemiluminescence. Fig. 7 shows the chemiluminescence of luminol with the previously applied two orifice configurations varying inlet pressure p_1 at constant temperatures. Because of the typically low intensity of the luminescence, the exposure time was set to $t_b = 10$ min. Additionally, a small amount of hydrogen peroxide was added to the solution to increase only intensity, but not the area of chemiluminescence.

The blue luminescence in the images of Fig. 7 show the area, which is relevant for oxidation processes. In this case, the luminescence gives an evidence of the area where the pollutants are degraded. The intensity and extend of the luminescence area rises with increasing inlet pressure for $d = 1$ mm and for $d = 1.7$ mm. Moreover, the area of chemiluminescence is wider at same pressure for $d = 1.7$ mm than for $d = 1$ mm since the volume flow is greater and thereby the more energy is provided. The change in chemiluminescence with varying orifice diameter and pressure follows the results from the cavitating jet length measurements.

Fig. 8 shows the comparison of the volume of chemiluminescence induced by cavitation for two different orifice diameters. Analogue to Fig. 5b, the fraction of the volume of chemiluminescence to the volume of the cavitation reactor is plotted over the hydraulic power P, as established in [48]. In the evaluation of these images, only the area is of interest and not the intensity distribution or luminous intensity.

Fig. 8 clearly shows a dependence on the applied power and the orifice diameter used. The greater the hydraulic power input, the greater the differences between the configurations. In comparison, especially at high-pressure levels larger volumes of chemiluminescence are obtained with the configuration $d = 1.7$ mm applying the same power. When comparing the results obtained in this study with those from [48], only slight differences can be seen. In most cases, the volume ratios from [48] are larger. Among other things, this is due to the fact that a more light-

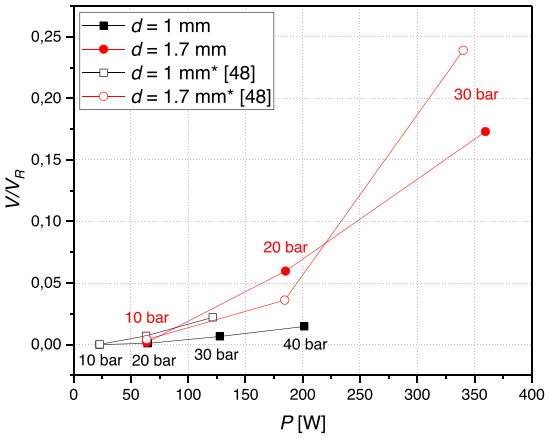

Fig. 8. Comparison of the strength of chemiluminescence of luminol induced by hydrodynamic cavitation for two different orifice configurations, d = 1 mm and d = 1.7 mm, as a function of hydraulic power P; at constant temperature of T = 20 °C varying pressure levels from Δp = 10 bar to Δp = 40 bar in steps of 10 (for d = 1.7 mm only Δp = 10 bar to Δp = 30 bar). V/V_R corresponds to the fraction of volume of chemiluminescence to the volume of the cavitation reactor. Points are connected linear. Comparison with results from literature [48].

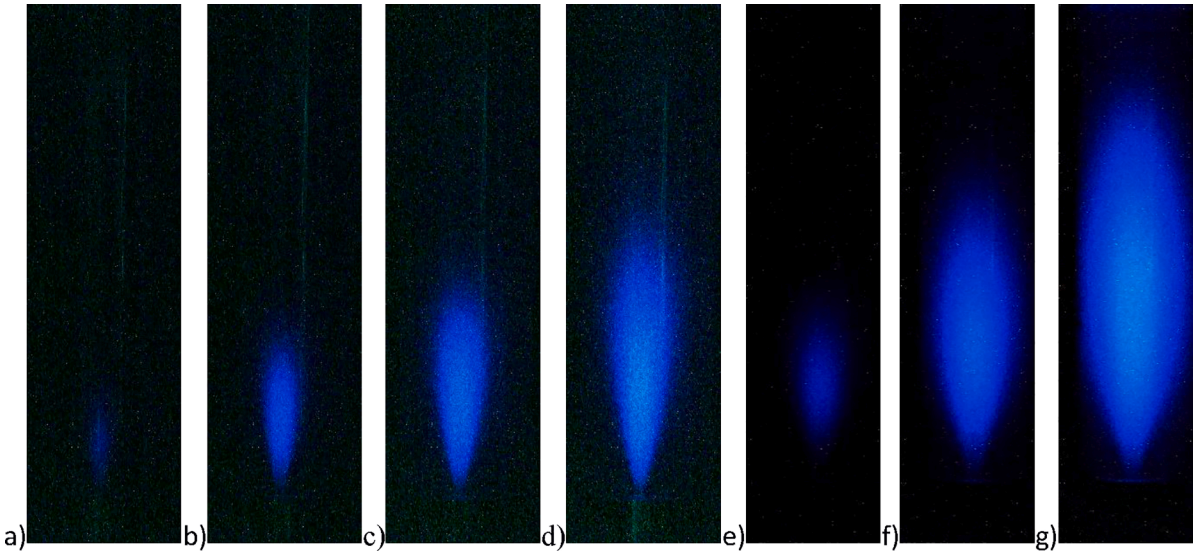

Fig. 7. Image section of the reactor chamber with chemiluminescence of luminol induced by hydrodynamic cavitation on rising pressure level Δp. Configuration d = 1 mm a)–d): a) Δp = 10 bar, b) Δp = 20 bar, c) Δp = 30 bar and d) Δp = 40 bar. Configuration d = 1.7 mm e)–g): e) Δp = 10 bar, f) Δp = 20 bar and g) Δp = 30 bar. Solution made of luminol $c_0 = 2$ g/l, hydrogen peroxide 1 ml (30%), pH 10, exposure time $t_b = 10$ min. Contrast and brightness in the images edited (different brightness for d = 1 mm and d = 1.7 mm in these images).

sensitive objective was used in [48] and the luminol solutions differed slightly. In principle, the curves have a similar tendency.

The volume of chemiluminescence is identical only in the low power range for both orifices. Similar to [48], there is one point, potentially a second, where similar volumes are achieved with the same hydraulic power input. The first point can be found for $d = 1$ mm at $\Delta p = 20$ bar and $d = 1.7$ mm at $\Delta p = 10$ bar. This point is now referred to operating point A. The second operating point can be assumed at $d = 1$ mm with $\Delta p = 30$ bar and $d = 1.7$ mm with $\Delta p = 15$ bar. This point is labelled as operating point B. Unfortunately, this point was not measured and does not exists for the configuration of $d = 1.7$ mm in Fig. 7. Nevertheless, in Fig. 5b, a similarity can be seen at the same power applied. These two operating points are further of interest when considering the BPA conversion rates, where the two orifices are used at same applied power and similar volume proportions of jet length and chemiluminescence. According to Fig. 6, the strong differences in bubble size and amount should then come to the focus.

However, it also becomes clear that the larger the orifice, the more activation energy is required for a reaction of luminol with hydroxyl radicals to appear in the form of chemiluminescence. The reason for this is that a larger orifice requires more power input to build up a comparable pressure, which in turn enables the necessary pressure lowering for the formation of cavitation.

The results of Fig. 8 are only conditionally comparable with the data from Fig. 5b regarding the volume ratios. Since the data from Fig. 5 are obtained by a threshold method from laser light section images, whereas the chemiluminescence images were captured with long-term exposure and were finally processed differently. It is also important to note that the experimental results obtained here are not comparable with those from [48], as the boundary conditions of the experimental arrangement differ in decisive points, e.g. objective lens, focus depth, solution mixture, temperature level. However, the evaluation methods are identical.

3.4. Degradation of bisphenol A by hydrodynamic cavitation

In this section, the experiments of BPA degradation by hydrodynamic cavitation are presented. The same configuration of optical measurements with identical orifices and pressure levels was applied in order to achieve comparability to aforementioned experiments. For the chemical analysis of the degradation, the water containing BPA was treated with $d = 1$ mm for $t_t = 90$ min and $d = 1.7$ mm for $t_t = 30$ min at pressure levels $\Delta p = \{10–30\}$ bar. The different treatment times were chosen to get comparable reactor passes for the different flow at the same pressure. In the process, seven samples were taken and analysed. The experiments for each operating point were performed three times revealing a deviation from mean value of 3–8%. To compare the different operating points, the rate constant of BPA degradation was determined after a treatment time of $t_t = 30$ min respectively $t_t = 90$ min using a pseudo first order kinetic. For the calculation of the pseudo first order kinetic, the following rate equation was applied

$$\ln\left(\frac{c(t)}{c(0)}\right) = -kt_t \tag{6}$$

with rate constant k, treatment time t_t and the initial concentration of BPA $c(0)$ as well as the concentration after the treatment $c(t)$. Fig. 9 displays the dependencies of BPA's degradation rate k on the pressure level Δp and the hydraulic power P.

For the investigated operating points and configurations BPA could successfully degraded by hydrodynamic cavitation. Fig. 9a shows that the rate constant k rises with increasing pressure level Δp for both orifices linear by trend. At $\Delta p = 5$ bar, a significant degradation of BPA was not possible to measure after the treatment time of $t_t = 30$ min.

The rate constant and its increase are clearly higher for $d = 1.7$ mm compared to $d = 1$ mm. This is due to the different amount of treated volume over time. Thus, after $t_t = 30$ min only $N_{VR} = 156$ reactor passes are reached with orifice $d = 1$ mm compared to $N_{VR} = 462$ passes with $d = 1.7$ mm. Because of this, the rate constant k is plotted against the hydraulic power P in Fig. 9b. The results of rate constants of both orifices show the same dependency against hydraulic power and seems to be roughly a linear function. Fig. 9b also shows that for the operating points investigated in this cavitation reactor, the conversion rate is not dependent to orifice geometry and the degradation is proportional to the hydraulic power applied. The reasons for a higher or lower degradation are discussed in Section 3.5 by adding the results of the optical methods to find correlations.

However, only the highest degradation points have been highlighted so far, although this does not have to be the most efficient state. Fig. 10 displays the ratio of $c(t)/c(0)$ plotted against energy E. This makes it possible to compare the energy required for the various configurations $c(t)/c(0)$. The configuration with minimum energy input at an arbitrary $c(t)/c(0)$ can be considered the most efficient. The energy E is calculated by Eq. (5), which involves volume flow, pressure difference and treatment time.

Fig. 10 illustrates the results of degradation to the applied energy for both orifice configurations. For $d = 1$ mm, seen in Fig. 10a, the most efficient pressure level is $\Delta p = 25$ bar, since the ratio of c/c_0 always is the lowest of all configurations by applying the same amount of energy. However, the difference between $\Delta p = \{20, 25, 30\}$ bar is not as significant as it shown in Fig. 10b for configuration $d = 1.7$ mm. The ratios

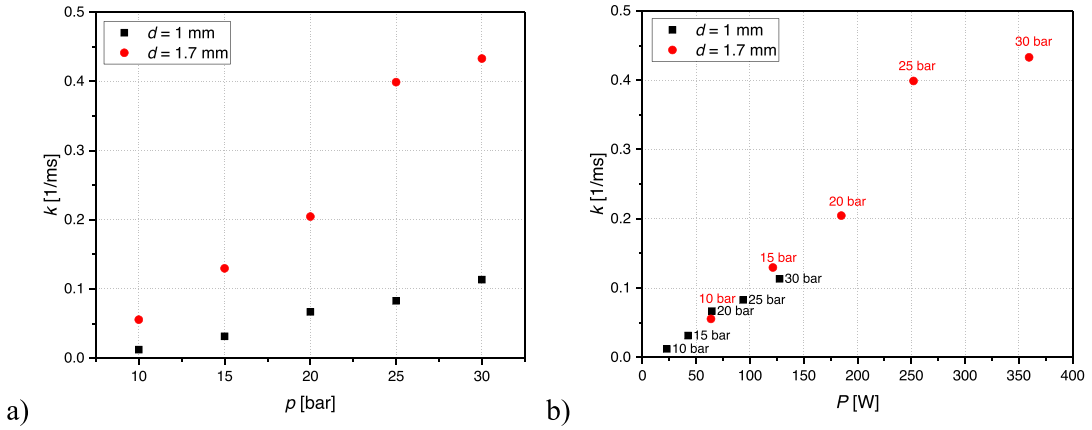

Fig. 9. Rate constants of BPA degradation calculated by first order kinetic for the configuration with d = 1 mm and d = 1.7 mm. a) Rate constant k against Δp = 10, 15, 20, 25 and 30 bar. b) Rate constants plotted against hydraulic power P calculated by pressure difference and related volume flow. BPA c(0) = 0.25 µmol/l, T = 20 °C, t_t = 30 min.

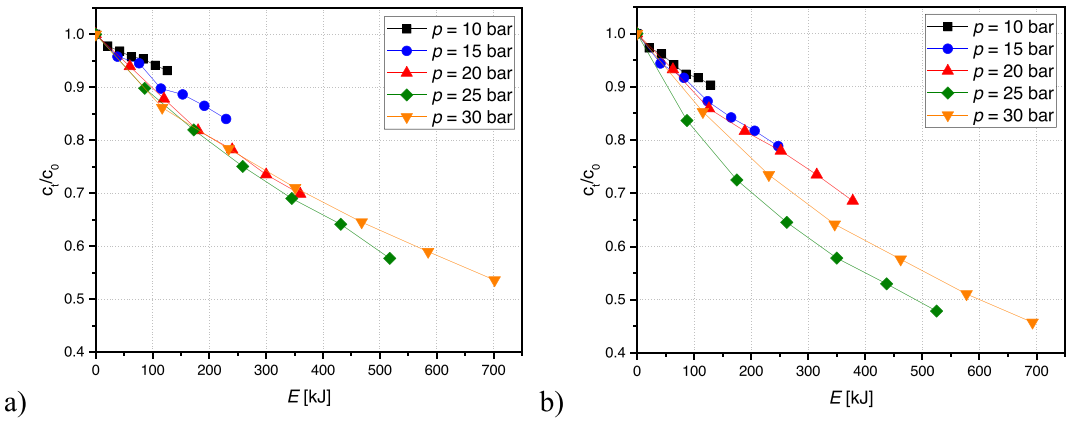

Fig. 10. Degradation of bisphenol A plotted by the ratio c(t)/c(0) against energy E. Energy is calculated by multiplying hydraulic power P with treatment time t_t. Different pressure levels of Δp = {10, 15, 20, 25, 30} bar are applied. a) Configuration d = 1 mm and b) d = 1.7 mm. BPA initial concentration is set to n = 0.25 μmol/l. T = 20 °C. Because of different pressure levels and orifices, reactor passes for diverse time are not same.

of degradation are lower for pressure below $\Delta p = 15$ bar. Comparing $d = 1$ mm and $d = 1.7$ mm, the degradation efficiency is better for the larger orifice at the same energy input. For the larger orifice, the best results are also achieved at $\Delta p = 25$ bar. As a result, using $d = 1.7$ mm, less energy has to be applied for $c/c_0 = 0.6$, which is equal to 40 percent of degradation. However, it becomes clear from the curves in Fig. 10b that with $d = 1.7$ mm at $\Delta p = 25$ bar and also $\Delta p = 30$ bar, significantly higher degradation rates are achieved compared to the other configurations at lower pressure levels.

Fig. 9 shows that for the operating points $d = 1$ mm at $\Delta p = 20$ bar and $d = 1.7$ mm at $\Delta p = 10$ bar, labelled as A in Table 2, similar rate constants can be determined for comparable hydraulic power. The same becomes noticeable for $d = 1$ mm $\Delta p = 30$ bar and $d = 1.7$ mm at $\Delta p =$ 15 bar, labelled as B. At these distinctive operating points, similar degradation rates are achieved by similar power consumption, indicating geometric independence. With the use of Fig. 10, the degradation rates can be compared to each other. The necessary energy at a fixed ratio c_t/c_0 for the interesting operating points can now be determined. Table 2 shows an overview of the energy input for a specific degradation for operating points A and B.

It can be seen that for point A with small orifice ($d = 1$ mm) less energy is required to achieve BPA degradation of 10 percent. Point B gives a similar result for BPA degradation of 20 percent, but the difference between both the orifices is lower compared to point A. This means that for conditions A and B, it is more efficient to achieve a certain degradation with a smaller orifice.

3.5. Correlation of the results by optical and chemical methods

In this section, the results of the optical measurements and the results of the degradation experiments of BPA are analysed for possible correlation. In order to answer the question concerning the similarity of the results achieved by the different methods, Fig. 11 shows the degradation of BPA in 100 reactor cycles over the normalized volume of the bubble cloud from Fig. 5b and over the chemiluminescence volume from Fig. 8.

The influence of different volume flows is eliminated by normalizing the degradation to 100 reactor passes. The treated volume is therefore the same, only the treatment time is different. Fig. 11 shows the curves for the two orifices that were investigated. At first, it is evident that with increasing inflow pressure the degradation as well as the volume determined by optical images increases.

Fig. 11a shows an increasing dependence between degradation and bubble field volume for $d = 1$ mm, whereas for $d = 1.7$ mm the increase reduces with increasing pressure. The shape of these plot is similar to Fig. 5b. The correlation of Figs. 5b and 11a let conclude that the degradation correlates with the applied power. The same can be stated for the degradation over the volume of chemiluminescence in Fig. 11b. Similar to Fig. 8, there are almost linear curves, whereby the increase with small orifice is considerably lower. In this dependency it is also noticeable that the degradation correlates with the power input.

This dependence is illustrated in Fig. 12. It is clearly visible that the smaller orifice with $d = 1$ mm requires less power than the large orifice with $d = 1.7$ mm in order to achieve a certain degradation for comparable volumes. The curve for $d = 1.7$ mm appears to be linear.

If the operating points A and B are compared with the configurations used in relation to the data in Fig. 12, it reveals that the degradation in point A with a smaller orifice for each power input is significantly higher than with $d = 1.7$ mm. The difference is about 6 percent. For point B, a nearly twice as high degradation is achieved with smaller orifice. This is due to the different size distribution and amount of bubbles. For the smaller orifice with smaller momentum and lower inertia to friction ratio, the bubble content affects more strongly the flow than for the larger orifice. In addition, the distance to the wall is greater, which leads to a less constrained formation of the jet. The highest degradation occurs in Fig. 12 for $d = 1$ mm at $\Delta p = 30$ bar. In this configuration, according to Fig. 6, a particularly large number of bubbles were detected, especially small bubbles and only a few large ones. The shape of the reaction area of chemiluminescence does not show an effect of the wall, so that the jet can propagate freely compared to the configuration $d = 1.7$ mm.

In summary, it can be stated that both bubble field expansion and luminol field expansion can predict the amount of degradation. In the examined configuration a linear dependence for the orifice $d = 1$ mm could be shown in Fig. 11a. For $d = 1.7$ mm, the curve is nonlinear due to the blocking effect caused by the reactor geometry. An interaction with the geometry is therefore an obstacle for a prognosis of degradation rates. The curves shown in Fig. 11b, on the other hand, are better suited for estimating the degradation. The extension of the volume of chemiluminescence with increasing pressure is well suited for a prediction of degradation due to the linear dependence. In addition, a prediction of

Table 2
Overview of the energy input for a specific BPA degradation in percent from Fig. 10 for the distinctive operating points A and B, each with different orifice diameters.

Operating condition	d in mm	Δp in bar	Degradation in % $[(1 - c_t/c_0)\cdot 100]$	E in kJ
A	1	20	10	100
	1.7	10		130
B	1	30	20	210
	1.7	15		240

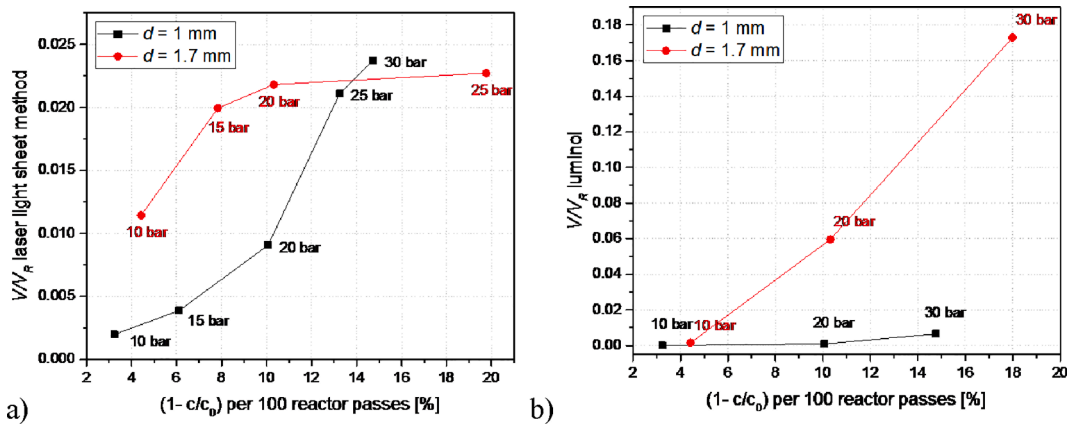

Fig. 11. Degradation of bisphenol A correlated to the results of the bubble optical measurements. a) Degradation of BPA at 100 reactor passes plotted over V/V_R from Fig. 5b. b) Degradation of BPA at 100 reactor passes plotted over the volume of chemiluminescence V/V_R from luminol experiments out of Fig. 8.

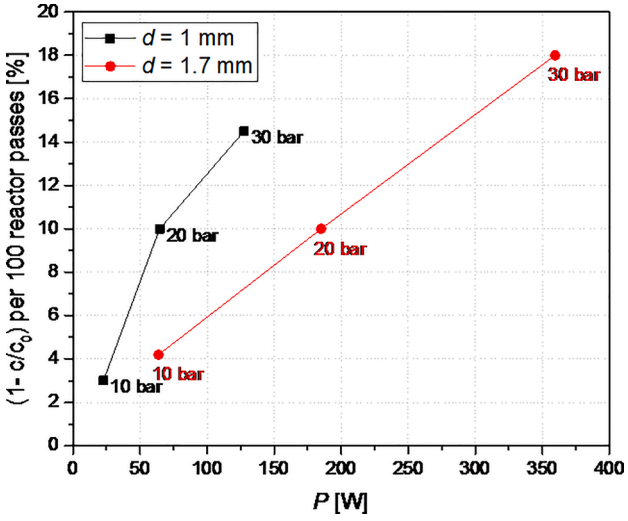

Fig. 12. Degradation of bisphenol A in percent correlated to the applied hydraulic power for d = 1 mm and d = 1.7 mm.

the degradation of bisphenol A based on the hydraulic power input is possible, based on the results of these study. Moreover, the results are also fruitful for further reactor design development, especially for oxidative degradation of pollutants in water.

4. Conclusion

In this study, the degradation of bisphenol A as a model for persistent organic water pollutants by hydrodynamic cavitation was evaluated and correlated to optical methods like laser light sheet images and luminol images. The laser light sheet images show the expansion of bubble field, whereas the luminol images offers information of areas of oxidising species. The range of inlet pressure for generating hydrodynamic cavitation was higher compared to other degradation studies in literature. With increasing pressure level from 10 to 30 bar more and smaller bubbles were generated and bubble field expansion increases linear by trend. The same results could be found for degradation experiments. With increasing pressure, the degradation of BPA was increased for both tested orifices. The results could be verified with luminol images. The area of sono-chemiluminescence increased with increasing pressure.

Based on degradation results and images of bubble field and luminol a correlation between the results can be achieved. An increase of bubble field area and sonochemiluminescence areas in luminol experiments are in line with the degradation experiments with BPA. A good correlation could be reached by luminol images because of the linear trend in the results. With higher pressure and higher fluid flow the reactor wall restricts the bubble field and this leads to a worse correlation at these conditions. Concurrently, a good correlation of power input and degradation results could be found. In case of efficiency, the smaller of the two orifices ($d = 1$ mm) needs less energy to achieve a certain degradation result, due to a larger amount of small bubbles and a full expansion of the jet unhindered by the reactor wall.

CRediT authorship contribution statement

Manuel Deggelmann: Conceptualization, Methodology, Validation, Formal analysis, Investigation, Writing – original draft, Writing – review & editing, Visualization, Project administration. **Julius-Alexander Nöpel:** Conceptualization, Methodology, Validation, Formal analysis, Investigation, Writing – original draft, Writing – review & editing, Visualization, Project administration. **Frank Rüdiger:** Resources, Writing – review & editing, Supervision, Project administration, Funding acquisition. **Dirk Paustian:** Writing – review & editing, Visualization. **Patrick Braeutigam:** Conceptualization, Resources, Writing – review & editing, Supervision, Project administration, Funding acquisition.

Declaration of Competing Interest

The authors declare that they have no known competing financial interests or personal relationships that could have appeared to influence the work reported in this paper.

Acknowledgement

This work was supported by the federal ministry for economic affairs and energy (BMWi) on the basis of a decision by the German Bundestag (16KN073422, ZF4050703RH6).

References

[1] X.-W. Luo, B. Ji, Y. Tsujimoto, A review of cavitation in hydraulic machinery, J. Hydrodyn. Ser. B 28 (2016) 335–358.
[2] P. Kumar, R.P. Saini, Study of cavitation in hydro turbines-A review, Renew. Sustain. Energ. Rev. 14 (1) (2010) 374–383.
[3] G. Kuiper, Cavitation Research and Ship Propeller Design, Appl. Sci. Res. 58 (1997) 33–50.
[4] S.S. Sawant, A.C. Anil, V. Krishnamurthy, C. Gaonkar, J. Kolwalkar, L. Khandeparker, D. Desai, A.V. Mahulkar, V.V. Ranade, A.B. Pandit, Effect of hydrodynamic cavitation on zooplankton: A tool for disinfection, Biochem. Eng. J. 42 (3) (2008) 320–328.
[5] J.-P. Franc, J.-M. Michel, Fundamentals of Cavitation, Fluid Mech. Appl. 76 (2005).

[6] R.A. Torres, F. Abdelmalek, E. Combet, C. Petrier, C. Pulgarin, A comparative study of ultrasonic cavitation and Fenton's reagent for bisphenol A degradation in deionised and natural waters, J. Hazard. Mater 146 (2007) 546.
[7] K.S. Suslick, M.M. Mdleleni, J.T. Ries, Chemistry Induced by Hydrodynamic Cavitation, J. Am. Chem. Soc. 119 (39) (1997) 9303–9304.
[8] W.H. Koppenol, J.F. Liebman, The oxidizing nature of the hydroxyl Radical. A comparison with the ferryl ion (FeO2+), J. Phys. Chem. 88 (1) (1984) 99–101.
[9] S. Gligorovski, R. Strekowski, S. Barbati, D. Vione, Environmental Implications of Hydroxyl Radicals (•OH), Chem. Rev. (Washington, DC, U. S.) 115 (2015) 13051-13092.
[10] C. Deng, G.L. Lu, M.F. Zhu, K. Li, J. Ma, H.B. Liu, Effective degradation of oil pollutants in water by hydrodynamic cavitation combined with electrocatalytic membrane, AIP Adv. 8 (2018), 125308.
[11] Z.M. Liu, M.F. Zhu, C. Deng, H. Su, P. Chen, Z. Wang, Pollutant and microorganism removal from water by hydrodynamic cavitation, Open Biotechnol. J. 10 (2016) 1.
[12] S. Parthasarathy, T. Siah Ying, S. Manickam, Generation and Optimization of Palm Oil-Based Oil-in-Water (O/W) Submicron-Emulsions and Encapsulation of Curcumin Using a Liquid Whistle Hydrodynamic Cavitation Reactor (LWHCR), Ind. Eng. Chem. Res. 52 (34) (2013) 11829–11837.
[13] B. Freudig, S. Tesch, H. Schubert, Production of Emulsions in High-Pressure Homogenizers – Part II: Influence of Cavitation on Droplet Breakup, Eng. Life Sci. 3 (6) (2003) 266–270.
[14] J. Ji, J. Wang, Y. Li, Y. Yu, Z. Xu, Preparation of biodiesel with the help of ultrasonic and hydrodynamic cavitation, Ultrasonics 44 (2006) e411–e414.
[15] K. Nakashima, Y. Ebi, N. Shibasaki-Kitakawa, H. Soyama, T. Yonemoto, Hydrodynamic Cavitation Reactor for Efficient Pretreatment of Lignocellulosic Biomass, Ind. Eng. Chem. Res. 55 (7) (2016) 1866–1871.
[16] Y.F. Wang, A.Y. Jia, Y. Wu, C.D. Wu, L.J. Chen, Disinfection of bore well water with chlorine dioxide/ sodium hypochlorite and hydrodynamic cavitation, Environ. Technol. 36 (2015) 479.
[17] S.S. Save, A.B. Pandit, J.B. Joshi, Use of hydrodynamic cavitation for large scale microbial cell disruption, Food Bioprod. Process. 75 (1997) 41.
[18] P. Thanekar, P.R. Gogate, Combined hydrodynamic cavitation based processes as an efficient treatment option for real industrial effluent, Ultrason. Sonochem. 53 (2019) 202–213.
[19] M. Dular, T. Griessler-Bulc, I. Gutierrez-Aguirre, E. Heath, T. Kosjek, A. Krivograd Klemenčič, M. Oder, M. Petkovšek, N. Rački, M. Ravnikar, A. Šarc, B. Širok, M. Zupanc, M. Žitnik, B. Kompare, Use of hydrodynamic cavitation in (waste)water treatment, Ultrason. Sonochem. 29 (2016) 577–588.
[20] N. Vedaraman, B.S. Shamshath, S.V. Srinivasan, Response surface methodology for decolourisation of leather dye using ozonation in a packed bed reactor, Clean Technol. Environ. Policy 15 (2013) 607.
[21] M. Deborde, S. Rabouan, P. Mazellier, J.-P. Duguet, B. Legube, Oxidation of bisphenol A by ozone in aqueous solution, Water Res. 42 (16) (2008) 4299–4308.
[22] K. Pirkanniemi, S. Metsarinne, M. Sillanpaa, Degradation of EDTA and novel complexing agents in pulp and paper mill process and waste waters by Fenton's reagent, J. Haz. Mater. 147 (1-2) (2007) 556–561.
[23] I. Ioan, S. Wilson, E. Lundanes, A. Neculai, Comparison of Fenton and sono-Fenton bisphenol A degradation, J. Hazard. Mater. 142 (1-2) (2007) 559–563.
[24] A. Ajmal, I. Majeed, R.N. Malik, H. Idriss, M.A. Nadeem, Principles and mechanisms of photocatalytic dye degradation on TiO2 based photocatalysts: a comparative overview, RSC Adv. 4 (70) (2014) 37003–37026.
[25] M. Muruganandham, M. Swaminathan, Photochemical oxidation of reactive azo dye with UV-H2O2 process, Food Bioprod. Process. 62 (2004) 269.
[26] Y. Tao, J. Cai, B. Liu, X. Huai, Z. Guo, Hydrodynamic cavitation in wastewater treatment: A review, Chem. Eng. Technol. 39 (2016) 1363–1376.
[27] N.N. Mahamuni, Y.G. Adewuyi, Advanced oxidation processes (AOPs) involving ultrasound for waste water treatment: A review with emphasis on cost estimation, Ultrason. Sonochem. 17 (6) (2010) 990–1003.
[28] R. Andreozzi, V. Caprio, A. Insola, R. Marotta, Advanced oxidation processes (AOP) for water purification and recovery, Catal. Today 53 (1999) 51–59.
[29] M. Franke, P. Braeutigam, Z.-L. Wu, Y. Ren, B. Ondruschka, Enhancement of chloroform degradation by the combination of hydrodynamic and acoustic cavitation, Ultrason. Sonochem. 18 (4) (2011) 888–894.
[30] J.-A. Nöpel, J. Fröhlich, F. Rüdiger, Experimental Investigation of Cavitation in a Jet Regarding Process Optimization, in: 11th International Symposium on Cavitation, Daejon, Korea, 2021.
[31] A. Šarc, T. Stepišnik-Perdih, M. Petkovšek, M. Dular, The issue of cavitation number value in studies of water treatment by hydrodynamic cavitation, Ultrason. Sonochem. 34 (2017) 51–59.
[32] J. Choi, M. Cui, Y. Lee, J. Kim, Y. Son, J. Khim, Hydrodynamic cavitation and activated persulfate oxidation for degradation of bisphenol A: Kinetics and mechanism, Chem. Eng. J. 338 (2018) 323–332.
[33] S. Gujar, P. Gogate, P. Kanthale, R. Pandey, S. Thakre, M. Agrawal, Combined oxidation processes based on ultrasound, hydrodynamic cavitation and chemical oxidants for treatment of real industrial wastewater from cellulosic fiber manufacturing sector, Sep. Purif. Technol. 257 (2021), 117888.
[34] P. Thanekar, P.R. Gogate, Improved processes involving hydrodynamic cavitation and oxidants for treatment of real industrial effluent, Sep. Purif. Technol. 239 (2020) 116563, https://doi.org/10.1016/j.seppur.2020.116563.
[35] N.P. Vichare, P.R. Gogate, A.B. Pandit, Optimization of hydrodynamic cavitation using a model reaction, Chem. Eng. Technol. 23 (8) (2000) 683–690.
[36] A.L. Prajapat, P.R. Gogate, Intensification of depolymerisation of aqueous guar gum using hydrodynamic cavitation, Chem. Eng. Process. 93 (2015) 1.
[37] P.R. Gogate, A.B. Pandit, A review and assessment of hydrodynamic cavitation as a technology for the future, Ultrason. Sonochem. 12 (2005) 21.
[38] P. Thanekar, P. Murugesan, P.R. Gogate, Improvement in biological oxidation process for the removal of dichlorvos from aqueous solutions using pretreatment based on Hydrodynamic Cavitation, J. Wat. Proc. Eng. 23 (2018) 20–26.
[39] S. Raut-Jadhav, V.K. Saharan, D. Pinjari, S. Sonawane, D. Saini, A. Pandit, Synergetic effect of combination of AOP's (hydrodynamic cavitation and H2O2) on the degradation of neonicotinoid class of insecticide, J. Hazard. Mater. 261 (2013) 139–147.
[40] V.K. Saharan, M.P. Badve, A.B. Pandit, Degradation of Reactive Red 120 dye using hydrodynamic cavitation, Chem. Eng. J. 178 (2011) 100–107.
[41] K.P. Mishra, P.R. Gogate, Intensification of degradation of Rhodamine B using hydrodynamic cavitation in the presence of additives, Sep. Purif. Technol. 75 (3) (2010) 385–391.
[42] M. Torabi Angaji, R. Ghiaee, Decontamination of unsymmetrical dimethylhydrazine waste water by hydrodynamic cavitation-induced advanced Fenton process, Ultrason. Sonochem. 23 (2015) 257–265.
[43] H. Soyama, J. Hoshino, Enhancing the aggressive intensity of hydrodynamic cavitation through a Venturi tube by increasing the pressure in the region where the bubbles collapse, AIP Adv. 6 (2016), 045113.
[44] M. Schlender, K. Minke, H.P. Schuchmann, Sono-chemiluminescence (SCL) in a high-pressure double stage homogenization processes, Chem. Eng. Sci. 142 (2016) 1–11.
[45] G.J. Price, N.K. Harris, A.J. Stewart, Direct observation of cavitation fields at 23 and 515 kHz, Ultrason. Sonochem. 17 (1) (2010) 30–33.
[46] U. Iben, F. Wolf, H.-A. Freudigmann, J. Fröhlich, W. Heller, Optical measurements of gas bubbles in oil behind a cavitating micro-orifice flow, Exp. Fluids 56 (2015) 114.
[47] H.-A. Freudigmann, U. Iben, P.F. Pelz, Air release measurements of V-oil 1404 downstream of a micro orifice at choked flow conditions, J. Phys.: Conf. Ser. 656 (2015) 012113, https://doi.org/10.1088/1742-6596/656/1/012113.
[48] J.-A. Nöpel, P. Zedler, M. Deggelmann, P. Braeutigam, J. Fröhlich, F. Rüdiger, Experimental investigation of the bubble distribution and chemical reactions induced by hydrodynamic cavitation inside a reactor-a preliminary study. Conference Proceedings 5th ICEFM, Munich, Germany, 2018, pp. 679–684, (2018).
[49] J. Im, C.W. Prevatte, S.R. Campagna, F.E. Löffler, Identification of 4-hydroxycumyl alcohol as the major MnO2-mediated bisphenol A transformation product and evaluation of its environmental fate, Environ. Sci. Technol. 49 (2015) 6214.
[50] D. Voutsa, P. Hartmann, C. Schaffner, W. Giger, Benzotriazoles, Alkylphenols and Bisphenol A in Municipal Wastewaters and in the Glatt River, Switzerland, Environ. Sci. Pollut. Res. 13 (5) (2006) 333–341.
[51] B.S. Rubin, Bisphenol A: An endocrine disruptor with widespread exposure and multiple effects, J. Steroid. Biochem. 127 (2011) 27–34.
[52] H.H. Le, E.M. Carlson, J.P. Chua, S.M. Belcher, Bisphenol A is released from polycarbonate drinking bottles and mimics the neurotoxic actions of estrogen in developing cerebellar neurons, Toxicol. Lett. 176 (2008) 149.
[53] S. Fukahori, H. Ichiura, T. Kitaoka, H. Tanaka, Capturing of bisphenol A photodecomposition intermediates by composite TiO2-zeolite sheets, Appl. Catal. B Environ. 46 (2003) 453.
[54] M. Dietrich, M. Franke, M. Stelter, P. Braeutigam, Degradation of endocrine disruptor bisphenol A by ultrasound-assisted electrochemical oxidation in water, Ultrason. Sonochem. 39 (2017) 741–749.
[55] G.V. Korshin, J. Kim, L. Gan, Comparative study of reactions of endocrine disruptors bisphenol A and diethylstilbestrol in electrochemical treatment and chlorination, Water Res. 40 (2006) 1070.
[56] R.A. Torres, C. Petrier, E. Combet, M. Carrier, C. Pulgarin, Ultrasonic cavitation applied to the treatment of bisphenol A. Effect of sonochemical parameters and analysis of BPA by-products, Ultrason. Sonochem. 15 (2008) 605.
[57] I. Gültekin, N.H. Ince, Ultrasonic destruction of bisphenol-A: The operating parameters, Ultrason. Sonochem. 15 (4) (2008) 524–529.
[58] G. Lu, L. Zhao, M. Zhu, C. Deng, H. Liu, Y.L.J. Ma, Effect of Cavitation Hydrodynamic Parameters on Bisphenol A Removal, Environ. Eng. Sci. 36 (2019) 8.
[59] J.L. Acero, S.B. Haderlein, T.C. Schmidt, M.J.F. Suter, U. von Gunten, MTBE Oxidation by Conventional Ozonation and the Combination Ozone/Hydrogen Peroxide: Efficiency of the Processes and Bromate Formation, Environ. Sci. Technol. 35 (2001) 4252–4259.
[60] H. Soyama, Cavitating Jet: A Review, Appl. Sci. 10 (2020) 7280.